

Abstract

The Main Ethiopian Rift (MER) is accompanied by extensive volcanism and the formation of geothermal systems, both having an imminent impact on lives of millions of local inhabitants. Although previous studies from the region found evidence that asthenospheric upwelling and associated decompression melting provide melt to magmatic mush systems that feed the tectono-volcanic segments in the rift valley, no geophysical model imaged these regional and local scale transcrustal structures within a single comprehensive 3-D model. To fill this gap, we combined regional and local magnetotelluric data sets to obtain the first multi-scale 3-D electrical conductivity model of the central MER. The model clearly images a magma ponding zone with up to 7 vol. % melt at the base of the crust in the western part of the rift, its connection to Aluto volcano via a tectonically controlled transcrustal magmatic mush system and how the melt, stored at shallow crustal depths, supplies heat for Aluto's geothermal system. Our model provides evidence that different volcano-tectonic lineaments in the rift valley share a common melt source, which has been debated in the past. The presented multi-scale model provides new constraints as well as geologic insights into the melt distribution below the rift and will facilitate future geothermal developments and volcanic hazard assessments in the MER.

Plain Language Summary

Continental rifting is a fundamental process of plate tectonics that breaks continents apart to ultimately form new oceans. The landscape of the Main Ethiopian Rift (MER) is characterized by abundant volcanism and hot springs, which indicate presence of geothermal resources formed by magmatic heating of subsurface water. In our study we present a 3-D subsurface image of the magmatic system and geothermal reservoir beneath Aluto volcano in the MER. The model shows the electrical conductivity distribution of the subsurface which allows us to infer the distribution of electrically conductive melt. This is the first model that provides a high-resolution image of the entire magmatic system below the MER from the deep magmatic melt source up to the surface. The new model images for the first time how geothermal reservoirs form as a consequence of rifting related volcanic activity thereby providing a clear illustration of fundamental geological processes. These results also have a high societal relevance by providing a basis for volcanic risk assessment and contributing to a better understanding of how the sustainable green geothermal energy resources form.

1 Introduction

The East African Rift System (EARS) is a prominent continental rift that shaped the landscape of East Africa, including the East African Plateau, rift valleys and numerous volcanoes. Rifting and rift-related volcanism in East Africa played a role in early human evolution (King & Bailey, 2006) and to this date affect the life of humans due to volcanic hazards (Biggs et al., 2021), but also by providing diverse climate conditions and rift-associated natural resources (Burnside et al., 2021; Kebede et al., 2020). A large number of studies, especially in the northern part of the EARS, the Main Ethiopian Rift (MER), have provided a wealth of information and knowledge on the geodynamic processes that initiated and drive rifting and associated volcanism in the EARS (e.g. Agostini et al., 2011a; Casey et al., 2006; Corti, 2009; Ebinger, 2005; Kendall et al., 2005; Kendall & Lithgow-Bertelloni, 2016; Keranen & Klemperer, 2008, and references therein).

One of the main findings of these studies is that neither mechanical stretching nor magmatic upwelling could be the the major driver of rifting alone, but it is a rather complex interplay between these processes (e.g. Beutel et al., 2010; Kendall et al., 2005). Active magmatism and volcanism in the MER is sustained by asthenospheric upwelling. The main hypothesis is that decompression melting occurs in the upper mantle, melt intrudes into the lithosphere, where it feeds magmatic dykes and sills leading to the formation of volcanic systems in the MER (Gallacher et al., 2016; Rychert et al., 2012). Petrological studies and geological mapping (Bonini et al., 2005; Keranen & Klemperer, 2008) from the central part of the MER (CMER) observed a correlation between the monogenetic vent distribution and fault systems (Fig. 1), which implies that a tectono-magmatic interplay drives the rifting. Multiple studies proposed that a complex magmatic system exists below the western, mostly aseismic, Silti Debre Zeyit Fault Zone (SDFZ) (Iddon & Edmonds, 2020; Mazzarini et al., 2013; Rooney et al., 2011), where the magma stalls and fractionates at multiple depths within the crust. In contrast, the eastern Wonji Fault Belt (WFB) is seismically more active (Keir et al., 2006), hosting most of the present-day crustal extension with well-developed magmatic pathways (Bilham et al., 1999; Mazzarini et al., 2013; Rooney et al., 2011). Magma rises quickly under the WFB and fractionates at low pressures corresponding to about 5 km depth (Gleeson et al., 2017; Iddon & Edmonds, 2020; Rooney et al., 2011). Along the WFB, long-lived silicic peralkaline volcanoes are found with shallow magma chambers that have undergone several phases of eruption and recharge (Fontijn et al., 2018). Active

82 magmatism and extensional strain along the WFB created ideal geological conditions for
83 the formation of high-temperature geothermal resources (e.g. Jolie et al., 2021).

84 However, there is still a lack of geophysical subsurface models for the MER that would
85 constrain the 3-D distribution of melt and image magmatic pathways across the continental
86 crust. Such geophysical subsurface images are critical for understanding controls on magma
87 transport, magma emplacement under rift-aligned segments and the formation of numerous
88 magma-driven geothermal systems in the MER (e.g. Jolie et al., 2021; Kebede et al.,
89 2020). The mindful exploitation of these geothermal resources would be beneficial for the
90 local society (IRENA, 2020). As a source of clean and renewable baseload energy, these
91 geothermal resources can satisfy the growing energy demand and sustain the local economic
92 growth. Numerous countries along the EARS plan to expand exploitation of renewable
93 geothermal energy resources (IRENA, 2020). Ethiopia is currently aiming at installing
94 1000 MWe of its estimated 10,000 MWe geothermal energy potential (Burnside et al., 2021;
95 Kebede et al., 2020).

96 Our study focuses on the area of Ethiopia's only producing geothermal power plant,
97 Aluto-Langano. The power plant is in operation since 1998 and has an installed capacity of
98 7.3 MWe (Kebede et al., 2020). Expansion work to reach 75 MWe is underway, with four new
99 wells having been drilled in 2022 (capitalethiopia.com, 2022). Our primary goal here is to
100 investigate the magmatic heat source of Aluto's geothermal system and how it is connected
101 to deeper lower crustal magmatic system. To this end, we will use the magnetotelluric (MT)
102 method and image 3-D electrical conductivity structure of the subsurface.

103 Previous MT and seismic studies from this region have identified electrical conduc-
104 tivity and shear wave velocity anomalies in the lower crust under the SDFZ (Hübert et
105 al., 2018; Kim et al., 2012; Samrock et al., 2015). These lower crustal seismic anomalies
106 have been interpreted as the lithospheric melt ponding zone. However, the lateral extent
107 of this anomaly and potential links to Aluto's magmatic reservoir under the WFB remain
108 poorly constrained. Further, it remains unclear whether volcanoes along the WFB and the
109 SDFZ are related to a common melt ponding zone or whether their magmas originate from
110 separated parental melt sources (e.g. Fig. 11 in Mazzarini et al., 2013; Rooney et al., 2011).

111 To address these questions and better constrain the structure below Aluto, we analyzed
112 a new MT dataset that covers both the rift and the Aluto volcanic complex. Our goal is to
113 obtain a new multi-scale 3-D electrical conductivity model of this area in the CMER (Fig. 1)

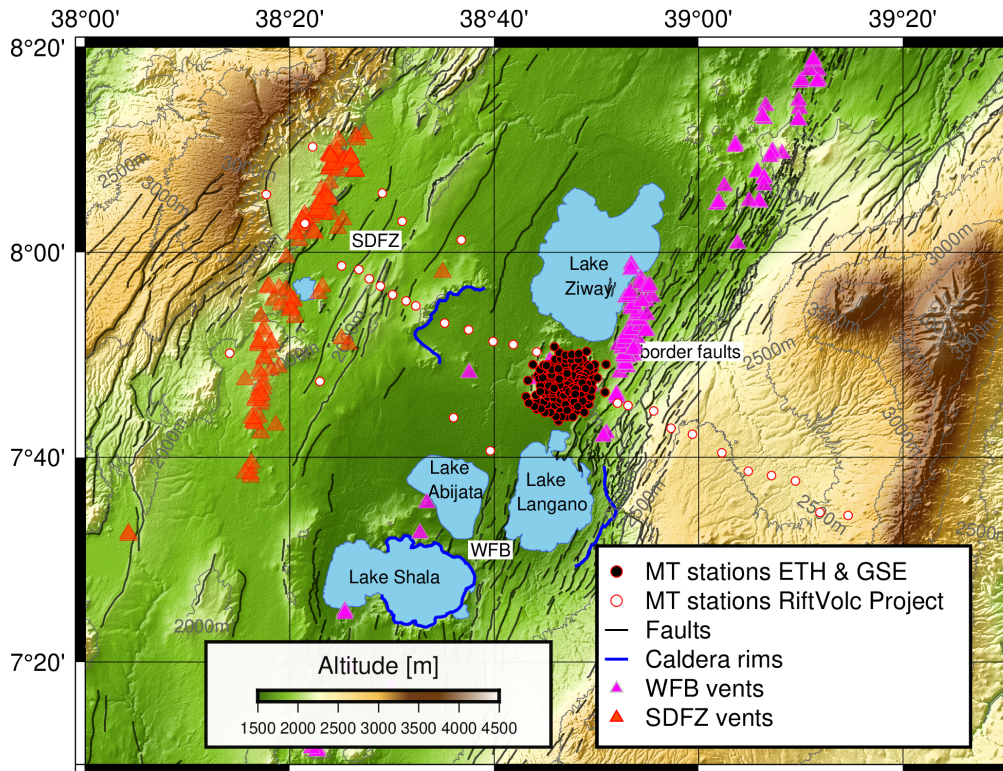


Figure 1. Study area in the Central Main Ethiopian Rift (CMER) with its faults systems (database of faults: Agostini et al., 2011b) and quaternary vents (grouped by Mazzarini & Isola, 2010). The vents belong to two different volcanic belts that are associated with the Wonji Fault Belt (WFB) and the Silti Debre Zeyit Fault Zone (SDFZ). Aluto volcano is located in the center of the study area in between the lakes Ziway and Langano. MT stations are coloured according to the institutions and projects that performed the measurement (MT-dataset by ETH Zurich (ETH) and Geological Survey of Ethiopia (GSE): Samrock et al. (2010) and MT-dataset by the RiftVolc Project: Hübert and Whaler (2020)). The survey area encompasses all fault systems of the CMER (WFB, SDFZ and border faults) and crosses the Gademotta caldera rim west of Aluto. The maximum difference in altitude along the profile is ≈ 1000 m.

114 and resolve both regional-scale structures in the lower crust and local structures related to
 115 Aluto's upper crustal magmatic and geothermal reservoirs.

116 2 Method and Data

117 To image the melt distribution across the rift and constrain the structures of Aluto's
 118 magmatic and geothermal reservoirs, we obtain the subsurface 3-D electrical conductivity
 119 distribution employing the (passive) magnetotelluric method (MT) (e.g. Cagniard, 1953).
 120 Broadband MT responses are sensitive to electrical conductivity structures across a wide

121 range of scales, providing a unique opportunity to study the subsurface from the surface
 122 down to the upper mantle. More details on the MT method are provided in the SI (Text S1).

123 2.1 Data

124 We combine data from regional and local MT surveys in the MER, as is shown in
 125 Fig. 1. The regional dataset, collected within the RiftVolc Project (Hübert & Whaler, 2020),
 126 consists of 33 MT stations that are distributed across the rift over a distance of 120 km with
 127 average site spacings between 4 km and 13 km (SI: Tab. S1). These regional-scale MT survey
 128 was supplemented by a local dataset of ETH and GSE (Samrock et al., 2010), consisting
 129 of 165 sites that cover the edifice of the Aluto volcano (15×15 km), with an average site
 130 spacing of 0.7 km. The MT transfer functions cover a period range of $T = 10^{-2} - 10^3$ s. For
 131 this period range and for the averaged electrical conductivity distribution in the study area,
 132 the penetration depth is calculated to range between 0.5 and 92.5 km, thereby providing a
 133 sufficient range for imaging both near-surface and crustal structures (SI: Fig. S2). Detailed
 134 information on the surveys and the collected MT data is provided in the SI (Text S2).

135 2.2 3-D Inversion

136 We used the GoFEM code to perform 3-D forward modelling and inversion (Arndt
 137 et al., 2020; Grayver, 2015; Grayver & Kolev, 2015). GoFEM uses locally refined meshes
 138 to facilitate multi-scale model parameterization (SI: Text S4) and accurately incorporate
 139 topography. The code was already used in earlier local-scale MT studies at Aluto (Samrock
 140 et al., 2020) and for multi-scale MT studies of volcanically active regions in Mongolia (Käuff
 141 et al., 2020).

142 Since impedance tensors are often affected by galvanic distortions, we first perform
 143 a phase tensor inversion. As the starting model for the phase tensor inversion, we used a
 144 homogeneous model with a resistivity of $\bar{\rho}_{a,ssq}^{1D} = 19.25 \Omega\text{m}$, where $\bar{\rho}_{a,ssq}^{1D}$ is the geometric
 145 mean of all observed apparent resistivities calculated from Z_{ssq} (SI: Eq. 6-11, see also Rung-
 146 Arunwan et al., 2016).

147 Although phase tensors are free of galvanic distortions (e.g. Caldwell et al., 2004),
 148 absolute values of electrical conductivity in models constrained solely by phase tensor data
 149 might be less constrained, especially when survey layout is sparse (Tietze et al., 2015). To
 150 mitigate this limitation, we ran the impedance tensor inversion and used the best-fitting

151 3-D phase tensor model as a starting model. By doing so, the impedance tensor inversion
152 is guided by the distortion-free phase tensor model and the negative impact of galvanic
153 distortions on the inversion is reduced. If there were no distortions and both phase and
154 impedance tensors contained the same information, we would expect the models to be
155 identical. In reality, the models exhibit some differences, mostly because the impedance
156 tensor inversion need to compensate for galvanic distortions by introducing some scattered
157 conductivity structures at shallow depths (Fig. 2 Samrock et al., 2018) (SI: Fig. S13).

158 Technical information on the inversion methodology and the achieved data fit for the
159 final phase and impedance tensor models is provided in the SI (Text S3 and S4). In what
160 follows, we will present the final impedance tensor model. The corresponding phase tensor
161 model is shown for completeness in the SI (Text S4.1).

162 **3 Results**

163 Both models, obtained from phase and impedance tensor inversions, fit the observed
164 data within the uncertainty ($\text{RMS} \leq 1$), given by the error-floor of 5 % applied row-wise to the
165 impedance tensor and propagated to the phase tensor (as in Käufel et al., 2018). Details about
166 the inversion progress and the achieved fit are provided in Fig. 2. Starting at an initial RMS
167 of 2.7, the phase tensor inversion converges to an RMS of 0.83 within four iterations. For
168 the subsequent impedance tensor inversion a relatively low model regularization is chosen,
169 as the large-scale structure is given by the phase tensor model, which is used as the starting
170 model for the impedance tensor inversion. Starting at an initial RMS of 5.1, the impedance
171 tensor inversion converges progressively until a final RMS of 0.81 is achieved (Fig. 2a). The
172 RMS distribution as a function of the period shows that shorter periods tend to yield lower
173 misfits than longer periods (Fig. 2b), which can be due to lower data quality at longer
174 periods. The normalized residuals of both obtained final models are uniformly distributed
175 and centered around zero, indicating that no systematic bias is present (Fig. 2c). More
176 detailed information about the model fit is provided in the SI (Text S5.2).

177 **3.1 Final model**

178 A cross-section through the final electrical conductivity model is shown in Fig. 3 a. An
179 approximately NW-SE-oriented vertical slice crosses the entire rift and traverses the center

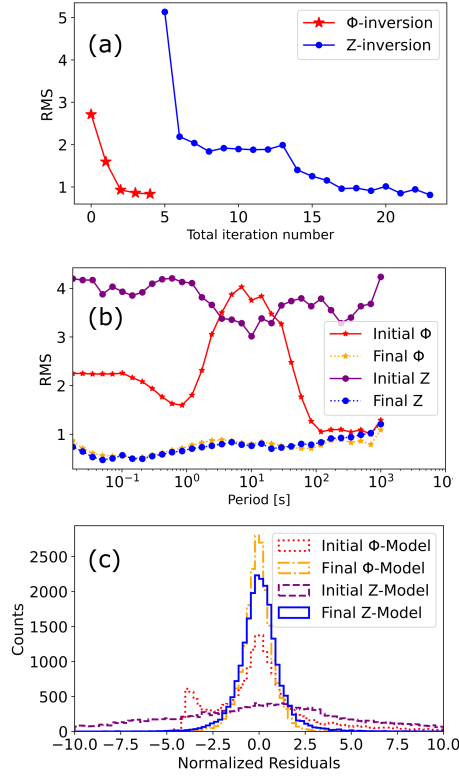


Figure 2. (a) RMS misfit during the phase tensor and the subsequent impedance tensor inversions. (b) RMS misfit versus period for the initial and final phase and impedance tensor inversion runs. (c) Residual distribution of initial and final phase tensor and impedance tensor models. Note that the final phase tensor model is used as a starting model for the impedance tensor inversion.

180 of Aluto volcano. Main electrical conductors (C) in the obtained multi-scale model are
 181 described in the following.

182 The largest conductivity anomaly in the model is the C3 conductor. The maximum
 183 recovered electrical conductivity within C3 is $\sigma = 0.18 \text{ S/m}$ (Fig. 3 a). The anomaly occupies
 184 a large volume in the lower crust under the western part of the rift and crosses the Moho
 185 boundary at depths of $z \approx 30 - 35 \text{ km b.s.l.}$ (Fig. 5). The lateral extent of C3 is about 50 km
 186 across the rift and 30 km along the rift, considering the 0.1 S/m isosurface (we note that
 187 data coverage along the rift axis is limited). It is evident that no high conductivity zone is
 188 found under the eastern part of the rift. C3 ends abruptly around the central rift axis and
 189 transitions into a continuously upward propagating channel denoted C2. The C2 structure
 190 is characterized by increased bulk electrical conductivities of $\sigma = 1.8 \text{ S/m}$ at depths of
 191 $z = 6 - 18 \text{ km b.s.l.}$. This channel terminates at a depth of $z = 4 \text{ km, b.s.l.}$ right below the
 192 Aluto volcano (Fig. 3 b). At shallower depths (down to about $z \approx 1.5 \text{ km}$ below surface), we

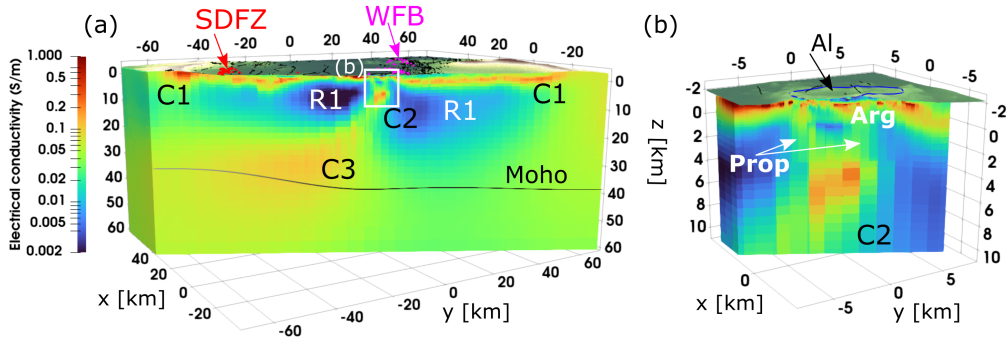


Figure 3. Final 3-D electrical conductivity model. (a) NW-SE oriented cross-section, covering the entire width of the CMER. The Moho boundary (black solid line) is taken from (Stuart et al., 2006). Pink and red triangles depict WFB and SDFZ vents, respectively (see also Fig. 1). Recovered structures are interpreted to be: (C1) Aquifer/sediment unit, (C2) magma ascent channel, (R1) solidified igneous rock and (C3) lower crustal melt ponding zone. The white box marks the area of the Aluto-Langano geothermal system (b). (b) Enlarged excerpt of the Aluto volcano (proposed caldera rim in blue). Increased conductivities in the shallow subsurface can be attributed to a clay cap, formed by argillic alteration (Arg) and higher-temperature propylitic alteration (Prop).

193 recover an electrically conductive layer (C1) that extends across the entire width of the rift,
 194 with bulk conductivity values of $\sigma = 0.1 - 0.5 \text{ S/m}$. This continuous layer (C1) is interrupted
 195 only under the edifice of Aluto volcano in the center of the shown cross-section (Fig. 3).

196 A large low-conductivity zone (R1) extends across the valley, with $\sigma \leq 0.01 \text{ S/m}$. R1
 197 is situated in the crust below the continuous conductive layer (C1) and is pierced by the
 198 conductive channel C2.

199 3.2 Interpretation

200 The presented electrical conductivity model is the first 3-D model of the CMER that
 201 images the transcrustal distribution of magma in sufficient detail to interpret it across scales
 202 from the lower crust to the surface. In what follows, we provide a geological interpretation of
 203 our 3-D electrical conductivity model (Figs. 3 and 5) taking in consideration earlier studies.

204 3.2.1 C3: Lower crustal magma ponding zone

205 We interpret this high conductivity anomaly to be caused by the presence of electrically
 206 conductive basaltic melt. Hence, C3 represents a zone of melt ponding at the base of

207 the crust. A quantitative melt fraction estimate within the C3 is given in Section 3.2.2.
208 The interpretation of C3 as a lower crustal melt ponding zone is supported by seismic
209 observations, geodynamic modelling studies and petrological models for melt evolution and
210 transport in the MER. In the following these studies are presented in more detail.

211 Analysis of seismic S to- P receiver functions provides evidence for a thinned lithosphere
212 and upwelling asthenosphere below the rift valley (Rychert et al., 2012). A pronounced low
213 seismic velocity anomaly is observed in the upwelling asthenosphere, which can only be
214 explained by presence of melt that originates from decompression melting (e.g. Chambers
215 et al., 2022; Kim et al., 2012; Rychert et al., 2012). It has been shown that the Moho
216 deepens from West to East in this area (Fig. 3), indicating that asthenospheric upwelling is
217 slightly asymmetric to the rift axis and more pronounced under the western part of the rift
218 (e.g. Keranen & Klemperer, 2008; Stuart et al., 2006). Geodynamic modelling by (Rychert
219 et al., 2012) shows that melt generated through decompression melting experiences strong
220 buoyancy forces causing it to migrate into the lower crust, where it accumulates in a melt
221 ponding zone above the Moho. The C3 structure in our model is spatially coherent with an
222 identified low shear wave velocity anomaly, that has been interpreted as such a melt ponding
223 reservoir (e.g. Chambers et al., 2022; Kim et al., 2012).

224 The observation that melt is asymmetrically distributed across the rift has also been
225 made by a regional MT study, approximately 110 km north of our study area (Whaler &
226 Hautot, 2006). There, authors report high electrical conductivities west of the rift-axis at a
227 depth of about 25 km.

228 That the lower crustal melt emplacement and asthenospheric upwelling occur asym-
229 metric with respect to the rift axis is not surprising. The tectonic analogue modelling has
230 suggested that the distribution of melt in the crust is guided by en-échelon structures, such
231 as the SDFZ and the WFB volcano-tectonic segments (Corti, 2009, and references therein).
232 However, it is interesting that lower crustal melt ponding is restricted to the area under
233 the SDFZ en-échelon segment, whereas no melt is ponding in the lower crust under the
234 WFB en-échelon segment, which is a much more active region in terms of volcano-tectonic
235 activity (e.g. Mazzarini et al., 2013). We suggest that the focusing of magma to the west
236 is likely caused by an "inherited" structure from the early rifting stage. In general, magma
237 emplacement during early stages of rifting could be dominated by a lateral squeezing of the
238 melt from the rift axis towards the border faults, as demonstrated by analogue modelling

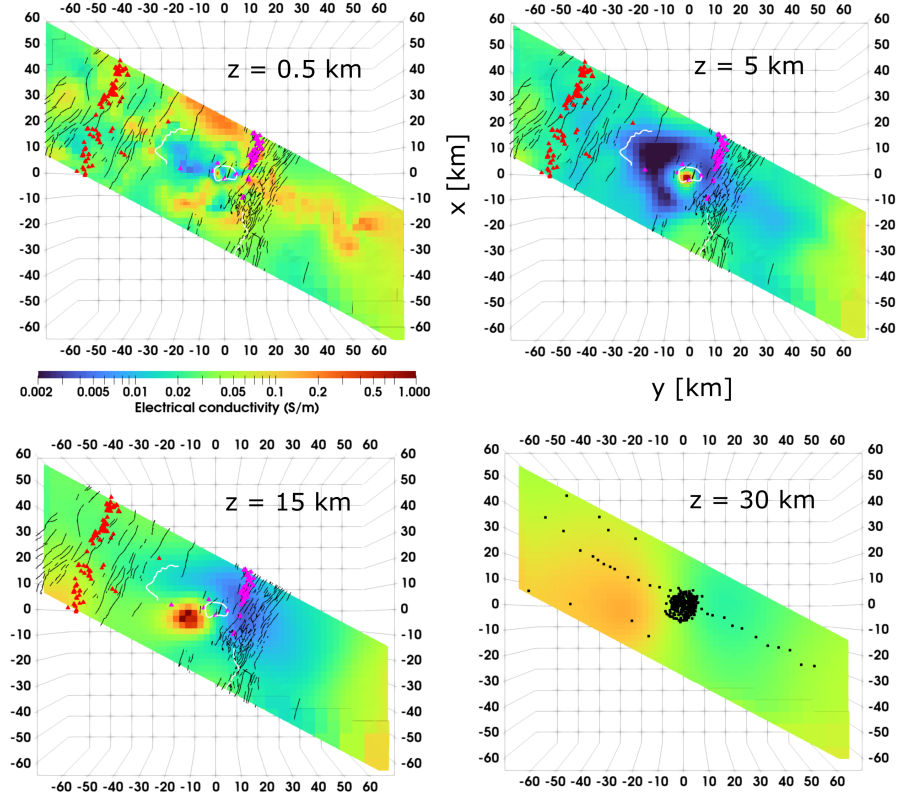


Figure 4. Horizontal slices at several depths from $z = 0.5 - 30$ km b.s.l. through the final impedance tensor model. It is evident from the figure that maximum electrical conductivities occur locally confined to the WSW of Aluto. Pink and red triangles depict WFB and SDFZ vents, respectively, black lines are faults and white lines are the western Gademotta caldera rim and the proposed Aluto caldera rim. Black dots on the 30 km b.s.l. depth slice indicate MT site locations.

239 studies (see Fig. 29 in Corti et al., 2003). Because rift development was asymmetric (e.g.
 240 Ebinger, 2005), with master border faults at the western side (e.g. in Corti et al., 2018,
 241 Fig. 2, profile 3), it is likely that the melt was favourably squeezed towards the western
 242 border faults, ultimately leading to the presently observed western asymmetric melt distri-
 243 bution. Hence, the observed asymmetric melt distribution is plausible, even though major
 244 present-day volcano-tectonic structures are found to the east of the rift axis.

245 Further, our electrical conductivity model suggests that the melt is not distributed
 246 uniformly along the imaged en-échelon segment of the SDFZ, rather the melt is focused
 247 in a region spatially confined to the WSW of Aluto (Fig. 4, Fig. 5). To the best of our
 248 knowledge, such detailed variations of along-rift melt distributions have not been resolved

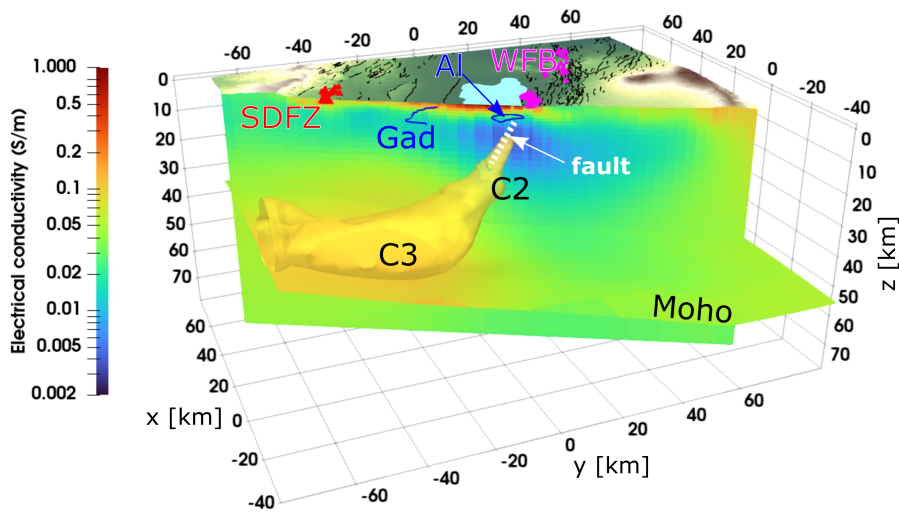


Figure 5. Vertical slice through the final model, approximately along the northern profile line of the MT sites (see Fig. 1). The Moho, as in Fig. 3, is colored by the electrical conductivities at the corresponding depth. The $\sigma = 0.1$ S/m-isosurface illustrates the extent of the magmatic ascent channel (C2) and the lower crustal melt ponding zone (C3). The magma ascent channel (C2) is situated exactly beneath Aluto and follows the dip angle of the WFB faults (65° ; Corti (2009)). The dipping of faults intersecting Aluto is indicated as a dashed white line. The melt ponding zone (C3) is confined to the area west of the rift-axis and WSW of Aluto volcano. Its lower bound roughly coincides with the Moho. Vents at the WFB and SDFZ are represented as red and pink triangles, respectively. The Gademotta (Gad) caldera rim is shown as a blue line, faults as black lines.

249 in the existing regional seismic models (e.g. Chambers et al., 2022; Kim et al., 2012). Our
 250 model indicates that lower crustal melt emplacement occurs much more punctuated and
 251 locally than previous geophysical models have shown and than tectonic analogue models
 252 have suggested (Corti, 2009, and references therein).

253 *3.2.2 Melt fraction estimates*

254 The model obtained from this study allows us to use electrical conductivity as an in-
 255 dependent constraint to quantify the amount of basaltic melt present in the lower crust.
 256 Until now, such estimates in the CMER relied mainly on seismic studies, of which some are
 257 summarized in the SI (Tab.S2). Adding electrical conductivity as an additional constraint
 258 reduces uncertainty of melt estimates and adds previously lacking knowledge on the spatial
 259 extent of the melt reservoir. To estimate the melt content, we used the experiment-calibrated
 260 model by Ni et al. (2011) (SI: Text S6), which parameterizes the electrical conductivity of

261 basaltic melt in terms of temperature and dissolved water content. The estimated tem-
 262 perature range for the primary basaltic melt within our interpreted source region (C3) is
 263 $\mathcal{T} = 1300 - 1400$ °C (SI: Tab. S2). Thermodynamic modelling of melt evolution constrains
 264 the dissolved water content within the parental basaltic melt of samples erupted at Aluto
 265 (Gleeson et al., 2017) to $c_{H_2O}^{melt} \leq 1$ wt%. This amount is well below the maximum wa-
 266 ter solubility of $\max(c_{H_2O}^{melt}) = 6.7$ wt% for identical magma storage conditions, which we
 267 calculated using MagmaSat by Ghiorso and Gualda (2015).

268 Under the relevant conditions (see SI: Tab. S2), the electrical conductivity of a basaltic
 269 melt is approximately $\sigma_{melt} = 2.9 - 8.4$ S/m (SI: Fig. S15). Based on the basaltic melt
 270 conductivity and the observed range of $\sigma_{bulk} = 0.1 - 0.18$ S/m in the magma ponding
 271 zone (C3), we calculate the melt fraction, using a modified Archie’s law (SI: Eq. 17 Glover,
 272 2015). The melt fraction is estimated for high melt-connectivities, reflected by a cementation
 273 exponent of $m = 1.15$, corresponding to the upper Hashin-Shtrikman bound, and lower
 274 connectivities, reflected by $m = 1.5$, which correspond to interstitial melt storage in a
 275 matrix of closely packed, perfect spheres (e.g. Glover, 2015). With these constraints, the
 276 melt fraction within the C3 conductor is 1.8–7.1 vol.% and 4.5–14.7 vol.% for maximum and
 277 minimum basaltic melt conductivities, respectively. Seismic studies estimated 2–7 vol.% of
 278 vertically aligned melt, based on modelling seismic velocities and seismic anisotropies in the
 279 uppermost mantle (Hammond & Kendall, 2016, SI: Tab. S2), fitting well into the range of
 280 our estimates. However, given the estimates from seismic studies, our maximum estimated
 281 melt fraction of 14.7 vol.% appears rather high. Taking into account that a melt fraction
 282 of 14.7 vol.% would be even higher than what has been estimated from a MT study in the
 283 Afar region (Desissa et al., 2013, SI: Tab. S2), where rifting is far more advanced and thus
 284 higher melt fractions are expected (e.g. Keranen & Klemperer, 2008). We consider our
 285 maximum estimate of 14.7 vol.%, and the underlying connectivity model, to be unrealistic,
 286 suggesting that higher temperatures, higher water contents and better melt connectivities
 287 are the conditions that better describe the in situ setting. In this case, our maximum
 288 estimated melt fraction is 7 vol.%. These estimated melt fractions are in agreement with
 289 independent estimates that are based on seismic velocities (see SI: Tab. S2) and support the
 290 interpretation of the C3 conductor to be a lower crustal magma ponding zone.

291 **3.2.3 C2: Transcrustal magma ascent channel**

292 We interpret the upward rising conductor C2 to be the magma ascent channel in
293 which melt migrates from the deeper melt ponding zone (C3) to the shallow magmatic
294 system beneath Aluto (Fig. 4, 5). The enhanced conductivity within C2 requires that melt
295 is present in the channel up to shallow depths of about 3 km b.s.l.. Hence, the upper part
296 of C2 also represents the magmatic heat source of Aluto's geothermal reservoir (Fig. 3 b).
297 The interpretation of C2 as a mature magmatic ascent channel is supported by petrological
298 studies, which predict that magma under the WFB rises quickly towards the surface, where
299 it either stalls and fractionates to eventually erupt as rhyolite, or the melt erupts quickly
300 as basalt (Mazzarini et al., 2013; Rooney et al., 2011). Another evidence for melt fractions
301 within C2 beneath Aluto is the observed aseismic zone in roughly the same area that was
302 interpreted as hot ductile crust (Wilks et al., 2020). The shallower part of channel C2 has
303 already been described by Samrock et al. (2020, 2021), who noted that the dip of the channel
304 ($\sim 65^\circ$) is coherent with the dominant fault plane of faults intersecting Aluto volcano. A
305 strong link between magmatic pathways and tectonically weak zones has been described by
306 numerous studies investigating magma-assisted continental rifting (e.g. Casey et al., 2006).
307 The close coupling between active tectonic structures and magma pathways in the central
308 MER is directly observable from the distribution of vents (Fig. 1), which shows that magma
309 preferentially rises along fault zones, where the crust has been weakened (e.g. Mazzarini et
310 al., 2013). The spatial conjunction of tectonic and magmatic features furthermore supports
311 the concept of "self-sustained" magmatic segments, where strain is preferentially localized
312 in magmatic segments, which promote intrusions (Beutel et al., 2010).

313 **3.2.4 R1: Solidified igneous rock**

314 The most striking feature of this electrical resistor is that it is clearly bounded to
315 the west by the Gademotta caldera rim (Fig. 4). The spatial correlation between R1 and
316 the Caldera rim leads us to the most plausible interpretation that R1 constitutes cooled
317 intrusive rock, as has already been previously suggested (Hübert et al., 2018; Samrock et
318 al., 2020). Its formation is likely related to the formation of the Gademotta caldera, where
319 volcanism ceased 1 Ma ago (Hutchison et al., 2016b).

320 **3.2.5 C1: Aquifer/sediment unit**

321 In agreement with the conceptual hydrogeological model of the study area by Ghiglieri
 322 et al. (2020), the conductor C1 images a shallow layer of pyroclastics and lavas that has been
 323 classified as a fissured aquifer. Considering reported groundwater electrical conductivities
 324 in the area (Burnside et al., 2021), the most widely distributed observed bulk conductivities
 325 within C1 ($\sigma = 0.1 - 0.2 \text{ S/m}$) would require an unreasonably large fluid fraction within
 326 C1 (see SI: Text S6.2). It is thus likely that enhanced conductivities in C1 are attributed
 327 to a superposition of ionic conduction in porous rocks and sediments as well as electrical
 328 conduction through conductive compounds such as clays, which also form through rock
 329 weathering processes and are commonly found in soils around the study area (Fritzsche et
 330 al., 2007).

331 **3.2.6 Geothermal system**

332 The shallow cap-like conductor ($\sigma = 0.1 - 0.3 \text{ S/m}$), shown in Fig. 3 b under Aluto vol-
 333 cano down to depths of 1.5 km below surface, and the underlying zone of decreased electrical
 334 conductivities ($\sigma = 0.02 \text{ S/m}$) between the cap and the upper part of the magma ascent
 335 channel C2 are typical features of volcano-hosted, high-temperature geothermal systems.
 336 The electrically conductive cap represents the argillic alteration zone, where electrically
 337 conductive clays are formed along the flow paths of circulating hot fluids on top of the con-
 338 vective hydrothermal reservoir, at temperatures of $\mathcal{T} \approx 80 - 180 \text{ }^\circ\text{C}$ (e.g. Kristmannsdottir,
 339 1979; Lévy et al., 2018). An electrically more resistive region under the clay cap represents
 340 the propylitic alteration zone, where less electrically conductive alteration minerals form
 341 at higher temperatures of $\mathcal{T} > 250 \text{ }^\circ\text{C}$. The C2 structure is the heat source that drives
 342 hydrothermal convection (Fig. 3 b). A more detailed description of the geothermal system
 343 can be found in previous local MT studies of the Aluto-Langano geothermal field (Cherkose
 344 & Mizunaga, 2018; Samrock et al., 2015, 2020).

345 **3.3 Discussion**

346 The electrical conductivity structure, revealed by our 3-D multi-scale model, is in
 347 agreement with the concept and models of magma-assisted continental rifting. A unique
 348 feature of our new 3-D model is that it images both the distribution of melt throughout the
 349 crust and the geothermal system. Based on this model and previous studies, we present an
 350 updated conceptual model of the central MER in Fig. 6.

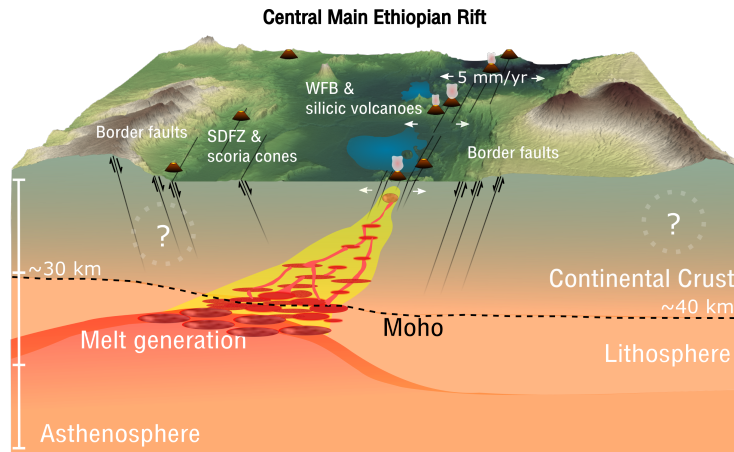


Figure 6. Conceptual model of the CMER. Asthenospheric upwelling leads to decompression melting. Buoyancy effects lead to upward migration of melt and melt ponding in the lower crust. Magma from the lower crustal ponding zone is fed into transcrustal magmatic mush systems that form along structural damage zones. A major part of the crustal extension (~ 5 mm/yr) occurs in the WFB (e.g. Bilham et al., 1999). The transcrustal magmatic system below the WFB is well developed. Here, magma rises quickly and fractionates in shallow magma reservoirs beneath silicic volcanoes, such as Aluto. The transcrustal magmatic system below the SDFZ is less mature and is not clearly imaged in this study. This might be caused by a lack of significant amounts of electrically conductive melt below the SDFZ, combined with a sparser MT site spacing in this area. Areas in the conceptual model that are less constrained by data are indicated by a question mark.

351 In general, magmatic underplating and ponding in stacked sills at the base of the
 352 crust, as is seen in our model (C3), is a widely adopted concept, but detailed imaging
 353 of such zones is rare (e.g. Cashman et al., 2017; Thybo & Artemieva, 2013). Analogue
 354 modelling has demonstrated that continental rifting undergoes an evolution during which
 355 magma first accumulates below border faults of the rift valley and is later focused towards
 356 en-échelon tectono-magmatic segments in the rift center (see Fig. 29 in Corti et al., 2003).
 357 Our model suggests that both stages of this evolution are still happening and influence the
 358 rift architecture, as the lower crustal ponding zone (C3) is asymmetric to the rift valley, close
 359 to western border faults, and as the magma ascent channel (C2) below the WFB follows the
 360 dip angle of the eastern border and the WFB faults.

361 Furthermore, the presented multi-scale model reconciles the concept of transcrustal
 362 magmatic mush systems, where magma storage happens at multiple interconnected levels
 363 in the crust, rather than in isolated voluminous magma chambers (e.g. Cashman et al.,
 364 2017). Indeed, in our model, magma accumulates in the lower crust (C3), where high tem-
 365 peratures maintain melt-bearing regions, even if the magma concentration is low. Segregated

366 magma migrates upwards along zones of crustal weaknesses to shallower crustal levels (C2),
367 where melt is stored in a smaller upper crustal reservoir (Fig. 3 b), which represents only the
368 small, uppermost part of a much larger magmatic system (Cashman et al., 2017). Hence
369 the WFB and the magma ascent channel (C2) form a well-developed tectono-magmatic sys-
370 tem that allows melt to rise quickly (e.g. Mazzarini et al., 2013; Rooney et al., 2011). In
371 contrast to the crustal structure below the WFB, our model does not show enhanced upper
372 crustal conductivities below the monogenetic vents in the western SDFZ region (Figs. 3,5).
373 Such anomalies could have been expected since C3 is the most obvious source of magma for
374 magmatic vents in the SDFZ. The absence of a significant electrical conductivity anomaly
375 under the SDFZ can be explained by the fact that ancient magma channels of the mono-
376 genetic vents are ephemeral and cooled quickly. If small amounts of melt are still present,
377 melt is probably stored in form of a highly crystalline and poorly interconnected mush and
378 is therefore more difficult to image, given the rather sparse distribution of MT stations in
379 this region. This is supported by petrological studies, which suggest that melt rises in a
380 complex dike system and is stored at multiple levels under the the SDFZ, where it cools
381 (e.g. Mazzarini et al., 2013; Rooney et al., 2011). The absence of significant amounts of melt
382 in the upper crust under SDFZ is also in agreement with the observed low seismic activity
383 beneath this area (Keir et al., 2006), which hints at much fewer or no ongoing intrusions in
384 that region. However, we note again that the 5 – 10 km site spacing in that area is much
385 larger than at Aluto and smaller-scale variations under the SDFZ might remain undetected
386 in our model. Despite the absence of significant conductivity anomalies in the upper crust
387 under the SDFZ, it is important to point out that volcanic activity in the SDFZ most likely
388 originates from the imaged deeper magmatic ponding zone (C3). Thus, our model suggests
389 that magmas, erupted at the SDFZ and at Aluto within the WFB, may come from a com-
390 mon magma source, which would be the lower crustal magma ponding zone (C3) in our
391 nomenclature. Although some geochemical studies have suggested spatially separated lower
392 crustal melt ponding zones for the volcanoes located along the fault zones of the SDFZ
393 and the WFB (e.g. Rooney et al., 2011), recent studies show that compositional variations
394 can be explained solely by different rates of magma ascent rather than by the existence of
395 distinct melt reservoirs (Nicotra et al., 2021).

396 Our current 3-D model differs in parts from the 2-D model by Hübert et al. (2018),
397 who performed a 2-D inversion of the 120 km long MT profile crossing Aluto (Fig. 1, see
398 SI: Tab. 1). (Hübert et al., 2018) imaged a strong conductivity anomaly below the SDFZ,

399 situated at much shallower depths than the lower magma ponding zone (C3) in our model.
400 Furthermore, the 2-D model of (Hübert et al., 2018) did not image a magma ascent channel
401 between the deeper source and the Aluto volcano. There can be several reasons for the
402 observed differences between the models. First, a large portion of the data exhibit 3-D
403 effects (see SI: Fig. S5) and, indeed, we observe significant conductivity variations along
404 the rift (Fig. 4), which demand and justify a 3-D modelling approach. Additionally, the
405 density of MT sites in our new study is significantly higher around Aluto, which can further
406 contribute to the observed differences.

407 **4 Conclusions and Outlook**

408 Our model provides a 3-D subsurface image of the Aluto volcano region in the MER and
409 reveals regional geological structures across the rift and a local geothermal system under
410 Aluto. The main contributions of this study concern the understanding of the magma-
411 assisted rifting of the MER and its geothermal systems, namely: (i) imaging the lower
412 crustal magmatic ponding zone with MT and thereby adding another geophysical constraint
413 (electrical conductivity) to its characterization and (ii) imaging, for the first time, the entire
414 volcano-hydrothermal system under Aluto, along with its connection to the deep-seated
415 lower crustal magma source.

416 The number of geophysical models imaging transcrustal magmatic mush systems at
417 this scale (e.g. Cashman et al., 2017) is still limited (e.g. Comeau et al., 2015; Hill et
418 al., 2022; Huang et al., 2015), especially when the setting of actively evolving continental
419 rifts is considered. Our detailed study provides previously missing geophysical evidence for
420 the hypothesized (e.g. Ebinger, 2005; Rooney et al., 2011) conceptual model of the CMER
421 (Fig. 6).

422 These observations, and the subsequent geological interpretation, were enabled by
423 combining regional and local MT datasets and by using a modern multi-scale magnetotelluric
424 imaging approach. Future regional-scale MT studies along the rift valley are required to
425 provide further insights into along-rift variations of the lower crustal magma ponding zone
426 (C3) and its connection to the volcanic geothermal centers of Tulu Moye and Corbetti,
427 where high-resolution MT surveys, comparable to Aluto, have been conducted (Gíslason et
428 al., 2015; Samrock et al., 2018).

Data availability

The MT data collected at Aluto by ETH Zurich are available from Samrock et al. (2010) via the IRIS EMTF Database: <http://ds.iris.edu/spud/emtf> under the Project entry "Ethiopia", and the survey name "Aluto-Langano Geothermal". The MT-dataset by project RiftVolc is available from Hübert and Whaler (2020) by DOI: 10.5285/2fb02ed4-5f50-4c14-aeec-27ee13aafc38. The MT data by the Geological Survey of Ethiopia are available for academic purposes on request from the Geological Survey of Ethiopia, as was the case for this study. The model will be made available for download in the ETH research collection (www.research-collection.ethz.ch) under Dambly et al. (2022) (DOI: 10.3929/ethz-b-000576313) in form of a Visualization Toolkit (VTK) data file for ParaView.

Declaration of competing interest

The authors declare that they have no known competing financial interests or personal relationships that could have appeared to influence the work reported in this paper.

CReDit Authorship statement

M.L.T.D. performed modelling and inversion of the magnetotelluric data, model visualization and developed numerical tools. F.S. contributed to the 3-D modelling and inversion of the data and model visualization. A.G. developed the GoFEM code and contributed to the 3-D modelling and inversion of the data. All authors interpreted the results and contributed to the writing and review of the paper.

Acknowledgments

M.L.T.D. was supported by ETH Grant ETH-02 19-1. A.G. was supported by the Heisenberg Grant from the German Research Foundation, Deutsche Forschungsgemeinschaft (Project No. 465486300). 3-D inversions and modelling were carried out at the Swiss National Supercomputing Center (CSCS) under project ID s1106. We thank Juliane Hübert and Kathy Whaler from Project RiftVolc and the Geological Survey of Ethiopia for making MT data available. We acknowledge the use of MTPy (Kirkby et al., 2019; Krieger & Peacock, 2014), Generic Mapping Tools (GMT), and Paraview, and thank NASA for providing SRTM digital elevation models. M.O.S., F.S. and M.L.T.D. thank the Werner Siemens

458 Foundation (Werner Siemens-Stiftung) for their endowment of the Geothermal Energy and
 459 Geofluids (GEG.ethz.ch) group at ETH Zurich.

460 References

- 461 Agostini, A., Bonini, M., Corti, G., Sani, F., & Manetti, P. (2011a). Distribution of
 462 quaternary deformation in the central Main Ethiopian Rift, East Africa. *Tectonics*,
 463 *30*(4), 1–21. doi: 10.1029/2010TC002833
- 464 Agostini, A., Bonini, M., Corti, G., Sani, F., & Manetti, P. (2011b). *Distribution of*
 465 *quaternary deformation in the central Main Ethiopian Rift, East Africa* [dataset].
 466 (Access Fault Dataset 2.5 <http://ethiopianrift.igg.cnr.it/utilities.htm>) doi:
 467 10.1029/2010TC002833
- 468 Arndt, D., Bangerth, W., Blais, B., Clevenger, T. C., Fehling, M., Grayver, A. V., ... Wells,
 469 D. (2020). The deal. II library, version 9.2. *Journal of Numerical Mathematics*, *28*(3),
 470 131–146. doi: 10.1515/jnma-2020-0043
- 471 Beutel, E., van Wijk, J., Ebinger, C., Keir, D., & Agostini, A. (2010). Formation and
 472 stability of magmatic segments in the Main Ethiopian and Afar Rifts. *Earth and*
 473 *Planetary Science Letters*, *293*(3-4), 225–235. doi: 10.1016/j.epsl.2010.02.006
- 474 Biggs, J., Ayele, A., Fischer, T. P., Fontijn, K., Hutchison, W., Kazimoto, E., ... Wright,
 475 T. J. (2021). Volcanic activity and hazard in the East African Rift zone. *Nature*
 476 *Communications*, *12*(1), 1–12. doi: 10.1038/s41467-021-27166-y
- 477 Bilham, R., Bendick, R., Larson, K., Mohr, P., Braun, J., Tesfaye, S., & Asfaw, L. (1999).
 478 Secular and tidal strain across the Main Ethiopian Rift. *Geophysical Research Letters*,
 479 *26*(18), 2789–2792. doi: 10.1029/1998GL005315
- 480 Bonini, M., Corti, G., Innocenti, F., Manetti, P., Mazzarini, F., Abebe, T., & Pecsckay, Z.
 481 (2005, February). Evolution of the Main Ethiopian Rift in the frame of Afar and
 482 Kenya rifts propagation. *Tectonics*, *24*(1). doi: 10.1029/2004TC001680
- 483 Burnside, N., Montcoudiol, N., Becker, K., & Lewi, E. (2021). Geothermal energy resources
 484 in Ethiopia: Status review and insights from hydrochemistry of surface and ground-
 485 waters. *Wiley Interdisciplinary Reviews: Water*, e1554. doi: 10.1002/wat2.1554
- 486 Cagniard, L. (1953, July). Basic theory of the magneto-telluric method of geophysical
 487 prospecting. *Geophysics*, *18*(3), 605–635. doi: 10.1190/1.1437915
- 488 Caldwell, T. G., Bibby, H. M., & Brown, C. (2004). The magnetotelluric phase tensor.
 489 *Geophysical Journal International*, *158*(2), 457–469. doi: 10.1111/j.1365-246X.2004

490 .02281.x

- 491 capitaethiopia.com. (2022). *Production tests kick start at Aluto Langano*.
 492 Retrieved from <https://www.capitaethiopia.com/capital/production-tests>
 493 [-kick-start-at-aluto-langano/](https://www.capitaethiopia.com/capital/production-tests-kick-start-at-aluto-langano/) (accessed 14 October 2022)
- 494 Casey, M., Ebinger, C. J., Keir, D., Gloaguen, R., & Mohamed, F. (2006). Strain ac-
 495 commodation in transitional rifts: Extension by magma intrusion and faulting in
 496 Ethiopian rift magmatic segments. *Environmental Geochemistry and Health, With*
 497 *Special Reference to Developing Countries*, 259(2003), 143–163. doi: 10.1144/
 498 GSL.SP.2006.259.01.13
- 499 Cashman, K. V., Sparks, R. S. J., & Blundy, J. D. (2017). Vertically extensive and unstable
 500 magmatic systems: A unified view of igneous processes. *Science*, 355(6331). doi:
 501 10.1126/science.aag3055
- 502 Chambers, E. L., Harmon, N., Rychert, C. A., Gallacher, R. J., & Keir, D. (2022, 04).
 503 Imaging the seismic velocity structure of the crust and upper mantle in the northern
 504 East African Rift using rayleigh wave tomography. *Geophysical Journal International*.
 505 doi: 10.1093/gji/ggac156
- 506 Cherkose, B. A., & Mizunaga, H. (2018). Resistivity imaging of Aluto-Langano geothermal
 507 field using 3-D magnetotelluric inversion. *Journal of African Earth Sciences*, 139,
 508 307-318. doi: 10.1016/j.jafrearsci.2017.12.017
- 509 Comeau, M. J., Unsworth, M. J., Ticona, F., & Sunagua, M. (2015). Magnetotelluric
 510 images of magma distribution beneath Volcán Uturuncu, Bolivia: Implications for
 511 magma dynamics. *Geology*, 43(3), 243–246. doi: 10.1130/G36258.1
- 512 Corti, G. (2009). Continental rift evolution: From rift initiation to incipient break-up in
 513 the Main Ethiopian Rift, East Africa. *Earth-Science Reviews*, 96(1-2), 1–53. doi:
 514 10.1016/j.earscirev.2009.06.005
- 515 Corti, G., Bonini, M., Conticelli, S., Innocenti, F., Manetti, P., & Sokoutis, D. (2003).
 516 Analogue modelling of continental extension: A review focused on the relations be-
 517 tween the patterns of deformation and the presence of magma. *Earth-Science Reviews*,
 518 63(3-4), 169–247. doi: 10.1016/S0012-8252(03)00035-7
- 519 Corti, G., Sani, F., Agostini, S., Philippon, M., Sokoutis, D., & Willingshofer, E. (2018). Off-
 520 axis volcano-tectonic activity during continental rifting: Insights from the transversal
 521 Goba-Bonga lineament, Main Ethiopian Rift (East Africa). *Tectonophysics*, 728-729,
 522 75–91. doi: 10.1016/j.tecto.2018.02.011

- 523 Dambly, M. L. T., Samrock, F., Grayver, A., & Saar, M. O. (2022). *Transcrustal 3-D*
 524 *electrical conductivity model of the Central Main Ethiopian Rift* [Model]. doi: 10.3929/
 525 ethz-b-000576313
- 526 Desissa, M., Johnson, N. E., Whaler, K. A., Hautot, S., Fisseha, S., & Dawes, G. J. (2013).
 527 A mantle magma reservoir beneath an incipient mid-ocean ridge in Afar, Ethiopia.
 528 *Nature Geoscience*, *6*(10), 861–865. doi: 10.1038/ngeo1925
- 529 Ebinger, C. (2005, 04). Continental break-up: The East African perspective. *Astronomy &*
 530 *Geophysics*, *46*(2), 2.16-2.21. doi: 10.1111/j.1468-4004.2005.46216.x
- 531 Fontijn, K., McNamara, K., Tadesse, A. Z., Pyle, D. M., Dessalegn, F., Hutchison, W.,
 532 ... Yirgu, G. (2018). Contrasting styles of post-caldera volcanism along the Main
 533 Ethiopian Rift: Implications for contemporary volcanic hazards. *Journal of Volcanol-*
 534 *ogy and Geothermal Research*, *356*, 90–113. doi: 10.1016/j.jvolgeores.2018.02.001
- 535 Fritzsche, F., Zech, W., & Guggenberger, G. (2007). Soils of the Main Ethiopian Rift valley
 536 escarpment: A transect study. *CATENA*, *70*(2), 209-219. doi: 10.1016/j.catena.2006
 537 .09.005
- 538 Gallacher, R. J., Keir, D., Harmon, N., Stuart, G., Leroy, S., Hammond, J. O., ... Ahmed,
 539 A. (2016). The initiation of segmented buoyancy-driven melting during continental
 540 breakup. *Nature Communications*, *7*, 1–9. doi: 10.1038/ncomms13110
- 541 Ghiglieri, G., Pistis, M., Abebe, B., Azagegn, T., Asresahagne Engidasew, T., Pittalis, D.,
 542 ... Haile, T. (2020). Three-dimensional hydrostratigraphical modelling supporting
 543 the evaluation of fluoride enrichment in groundwater: Lakes basin (Central Ethiopia).
 544 *Journal of Hydrology: Regional Studies*, *32*, 100756. doi: 10.1016/j.ejrh.2020.100756
- 545 Ghiorso, M. S., & Gualda, G. A. (2015). An H₂O–CO₂ mixed fluid saturation model
 546 compatible with rhyolite-MELTS. *Contributions to Mineralogy and Petrology*, *169*(6),
 547 1–30. doi: 10.1007/s00410-015-1141-8
- 548 Gíslason, G., Eysteinnsson, H., Björnsson, G., & Hardardóttir, V. (2015). Results of surface
 549 exploration in the Corbetti geothermal area, Ethiopia. In *Proceedings world geothermal*
 550 *congress*. Melbourne, Australia.
- 551 Gleeson, M. L., Stock, M. J., Pyle, D. M., Mather, T. A., Hutchison, W., Yirgu, G., &
 552 Wade, J. (2017). Constraining magma storage conditions at a restless volcano in
 553 the Main Ethiopian Rift using phase equilibria models. *Journal of Volcanology and*
 554 *Geothermal Research*, *337*, 44–61. doi: 10.1016/j.jvolgeores.2017.02.026
- 555 Glover, P. (2015, April). Geophysical properties of the near surface Earth: Electrical

- 556 properties. In G. Schubert (Ed.), *Treatise on geophysics* (Second ed., pp. 89–137).
 557 Elsevier Oxford. doi: 10.1016/B978-0-444-53802-4.00189-5
- 558 Grayver, A. V. (2015). Parallel three-dimensional magnetotelluric inversion using adap-
 559 tive finite-element method. part i: Theory and synthetic study. *Geophysical Journal*
 560 *International*, 202(1), 584–603. doi: 10.1093/gji/ggv165
- 561 Grayver, A. V., & Kolev, T. V. (2015). Large-scale 3D geoelectromagnetic modeling using
 562 parallel adaptive high-order finite element method. *Geophysics*, 80(6), E277–E291.
 563 doi: 10.1190/geo2015-0013.1
- 564 Hammond, J. O., & Kendall, J. M. (2016). Constraints on melt distribution from seismology:
 565 A case study in Ethiopia. *Environmental Geochemistry and Health, With Special*
 566 *Reference to Developing Countries*, 420(1), 127–147. doi: 10.1144/SP420.14
- 567 Hill, G. J., Wannamaker, P. E., Maris, V., Stodt, J. A., Kordy, M., Unsworth, M. J., ...
 568 Kyle, P. (2022). Trans-crustal structural control of CO₂-rich extensional magmatic
 569 systems revealed at Mount Erebus Antarctica. *Nature Communications*, 13(1), 1–10.
 570 doi: 10.1038/s41467-022-30627-7
- 571 Huang, H.-H., Lin, F.-C., Schmandt, B., Farrell, J., Smith, R. B., & Tsai, V. C. (2015).
 572 The Yellowstone magmatic system from the mantle plume to the upper crust. *Science*,
 573 348(6236), 773–776. doi: 10.1126/science.aaa5648
- 574 Hübner, J., & Whaler, K. (2020). *Magnetotelluric and transient electromagnetic data from*
 575 *the Main Ethiopian Rift. British Geological Survey. (dataset)*. [dataset]. doi: 10.5285/
 576 2fb02ed4-5f50-4c14-aec-27ee13aafc38
- 577 Hübner, J., Whaler, K., & Fisseha, S. (2018). The electrical structure of the central Main
 578 Ethiopian Rift as imaged by magnetotellurics: Implications for magma storage and
 579 pathways. *Journal of Geophysical Research, Solid Earth*, 123(7), 6019–6032. doi:
 580 10.1029/2017JB015160
- 581 Hutchison, W., Biggs, J., Mather, T. A., Pyle, D. M., Lewi, E., Yirgu, G., ... Fischer,
 582 T. P. (2016b). Causes of unrest at silicic calderas in the East African Rift: New con-
 583 straints from InSAR and soil-gas chemistry at Aluto volcano, Ethiopia. *Geochemistry,*
 584 *Geophysics, Geosystems*, 17(8), 3008–3030. doi: 10.1002/2016GC006395
- 585 Iddon, F., & Edmonds, M. (2020). Volatile-rich magmas distributed through the upper
 586 crust in the Main Ethiopian Rift. *Geochemistry, Geophysics, Geosystems*, 21(6). doi:
 587 10.1029/2019GC008904
- 588 IRENA. (2020). *Geothermal development in Eastern Africa: Recommendations for power*

- 589 *and direct use*. Abu Dhabi: International Renewable Energy Agency.
- 590 Jolie, E., Scott, S., Faulds, J., Chambefort, I., Axelsson, G., Gutiérrez-Negrín, L. C., ...
591 Zemedkun, M. T. (2021). Geological controls on geothermal resources for power
592 generation. *Nature Reviews Earth & Environment*, *2*(5), 324–339. doi: 10.1038/
593 s43017-021-00154-y
- 594 Käüfl, J. S., Grayver, A. V., Comeau, M. J., Kuvshinov, A. V., Becken, M., Kamm, J.,
595 ... Demberel, S. (2020). Magnetotelluric multiscale 3-D inversion reveals crustal
596 and upper mantle structure beneath the Hangai and Gobi-Altai region in Mongolia.
597 *Geophysical Journal International*, *221*(2), 1002–1028. doi: 10.1093/gji/ggaa039
- 598 Käüfl, J. S., Grayver, A. V., & Kuvshinov, A. V. (2018). Topographic distortions of
599 magnetotelluric transfer functions: A high-resolution 3-D modelling study using real
600 elevation data. *Geophysical Journal International*, *215*(3), 1943–1961. doi: 10.1093/
601 gji/ggy375
- 602 Kebede, S., Fikru, W., & Tesfaye, K. (2020). Status of geothermal exploration and devel-
603 opment in Ethiopia. In *Proceedings world geothermal congress*.
- 604 Keir, D., Ebinger, C. J., Stuart, G. W., Daly, E., & Ayele, A. (2006). Strain accommodation
605 by magmatism and faulting as rifting proceeds to breakup: Seismicity of the northern
606 Ethiopian Rift. *Journal of Geophysical Research, Solid Earth*, *111*(5), 1–17. doi:
607 10.1029/2005JB003748
- 608 Kendall, J.-M., & Lithgow-Bertelloni, C. (2016). Why is Africa rifting? *Environmental*
609 *Geochemistry and Health, With Special Reference to Developing Countries*, *42*(1),
610 11–30. doi: 10.1144/SP420.17
- 611 Kendall, J.-M., Stuart, G., Ebinger, C., Bastow, I., & Keir, D. (2005, January). Magma-
612 assisted rifting in Ethiopia. *Nature*, *433*(7022), 146–148. doi: 10.1038/nature03161
- 613 Keranen, K., & Klemperer, S. L. (2008). Discontinuous and diachronous evolution of the
614 Main Ethiopian Rift: Implications for development of continental rifts. *Earth and*
615 *Planetary Science Letters*, *265*(1-2), 96–111. doi: 10.1016/j.epsl.2007.09.038
- 616 Kim, S., Nyblade, A. A., Rhie, J., Baag, C. E., & Kang, T. S. (2012). Crustal S-wave velocity
617 structure of the Main Ethiopian Rift from ambient noise tomography. *Geophysical*
618 *Journal International*, *191*(2), 865–878. doi: 10.1111/j.1365-246X.2012.05664.x
- 619 King, G., & Bailey, G. (2006). Tectonics and human evolution. *Antiquity*, *80*(308), 265–286.
620 doi: 10.1017/S0003598X00093613
- 621 Kirkby, A. L., Zhang, F., Peacock, J., Hassan, R., & Duan, J. (2019). The MTPy software

- 622 package for magnetotelluric data analysis and visualisation. *Journal of Open Source*
623 *Software*, 4(37), 1358. doi: 10.21105/joss.01358
- 624 Krieger, L., & Peacock, J. R. (2014). MTPy: A python toolbox for magnetotellurics.
625 *Computers & Geosciences*, 72, 167-175. doi: 10.1016/j.cageo.2014.07.013
- 626 Kristmannsdottir, H. (1979). Alteration of basaltic rocks by hydrothermal-activity at
627 100-300°C. In M. Mortland & V. Farmer (Eds.), *International clay conference 1978*
628 (Vol. 27, p. 359-367). Elsevier. doi: 10.1016/S0070-4571(08)70732-5
- 629 Lévy, L., Gibert, B., Sigmundsson, F., Flóvenz, O. G., Hersir, G. P., Briole, P., & Pezard,
630 P. A. (2018). The role of smectites in the electrical conductivity of active hydrothermal
631 systems: Electrical properties of core samples from Krafla volcano, Iceland. *Geophys-*
632 *ical Journal International*, 215(3), 1558–1582. doi: 10.1093/gji/ggy342
- 633 Mazzarini, F., & Isola, I. (2010). Monogenetic vent self-similar clustering in extending
634 continental crust: Examples from the East African Rift system. *Geosphere*, 6(5),
635 567–582. doi: 10.1130/GES00569.1
- 636 Mazzarini, F., Rooney, T. O., & Isola, I. (2013). The intimate relationship between strain
637 and magmatism: A numerical treatment of clustered monogenetic fields in the Main
638 Ethiopian Rift. *Tectonics*, 32(1), 49–64. doi: 10.1029/2012TC003146
- 639 Ni, H., Keppler, H., & Behrens, H. (2011). Electrical conductivity of hydrous basaltic melts:
640 Implications for partial melting in the upper mantle. *Contributions to Mineralogy and*
641 *Petrology*, 162(3), 637–650. doi: 10.1007/s00410-011-0617-4
- 642 Nicotra, E., Viccaro, M., Donato, P., Acocella, V., & De Rosa, R. (2021). Catching the Main
643 Ethiopian Rift evolving towards plate divergence. *Scientific Reports*, 11(1), 1–16. doi:
644 10.1038/s41598-021-01259-6
- 645 Rooney, T. O., Bastow, I. D., & Keir, D. (2011). Insights into extensional processes during
646 magma assisted rifting: Evidence from aligned scoria cones. *Journal of Volcanology*
647 *and Geothermal Research*, 201(1-4), 83–96. doi: 10.1016/j.jvolgeores.2010.07.019
- 648 Rung-Arunwan, T., Siripunvaraporn, W., & Utada, H. (2016). On the Berdichevsky average.
649 *Physics of the Earth and Planetary Interiors*, 253, 1–4. doi: 10.1016/j.pepi.2016.01
650 .006
- 651 Rychert, C. A., Hammond, J. O., Harmon, N., Michael Kendall, J., Keir, D., Ebinger, C., . . .
652 Stuart, G. (2012). Volcanism in the Afar Rift sustained by decompression melting with
653 minimal plume influence. *Nature Geoscience*, 5(6), 406–409. doi: 10.1038/ngeo1455
- 654 Samrock, F., Grayver, A. V., Bachmann, O., Karakas, Ö., & Saar, M. O. (2021). Integrated

- 655 magnetotelluric and petrological analysis of felsic magma reservoirs: Insights from
 656 Ethiopian rift volcanoes. *Earth and Planetary Science Letters*, 559, 116765. doi:
 657 10.1016/j.epsl.2021.116765
- 658 Samrock, F., Grayver, A. V., Cherkose, B., Kuvshinov, A., & Saar, M. O. (2020, October).
 659 Aluto-Langano geothermal field, Ethiopia: Complete image of underlying magmatic-
 660 hydrothermal system revealed by revised interpretation of magnetotelluric data. In
 661 *Proceedings world geothermal congress (wgc 2020+1)* (p. 11054). Reykjavic, Iceland.
 662 doi: 10.3929/ethz-b-000409980
- 663 Samrock, F., Grayver, A. V., Eysteinnsson, H., & Saar, M. O. (2018). Magnetotelluric
 664 image of transcrustal magmatic system beneath the Tulu Moye geothermal prospect
 665 in the Ethiopian Rift. *Geophysical Research Letters*, 45(23), 12–847. doi: 10.1029/
 666 2018GL080333
- 667 Samrock, F., Kuvshinov, A., Bakker, J., Jackson, A., & Fisseha, S. (2015). 3-D analysis
 668 and interpretation of magnetotelluric data from the Aluto-Langano geothermal field,
 669 Ethiopia. *Geophysical Journal International*, 202(3), 1923–1948. doi: 10.1093/gji/
 670 ggv270
- 671 Samrock, F., Kuvshinov, A., Bakker, J., Jackson, A., Fisseha, S., staff of Addis Ababa Uni-
 672 versity, & the Geological Survey of Ethiopia. (2010). *Magnetotelluric and ver-*
 673 *tical magnetic transfer functions acquired at the Aluto-Langano geothermal field,*
 674 *Ethiopia* [dataset]. (from the IRIS database, <http://ds.iris.edu/spud/emtf>) doi:
 675 10.17611/DP/EMTF/ETHIOPIA/ETHZ
- 676 Stuart, G., Bastow, I., & Ebinger, C. (2006). Crustal structure of the northern main
 677 ethiopian rift from receiver function studies. *Geological Society, London, Special Pub-*
 678 *lications*, 259(1), 253–267. doi: 10.1144/GSL.SP.2006.259.01.20
- 679 Thybo, H., & Artemieva, I. (2013). Moho and magmatic underplating in continental
 680 lithosphere. *Tectonophysics*, 609, 605–619. doi: 10.1016/j.tecto.2013.05.032
- 681 Tietze, K., Ritter, O., & Egbert, G. D. (2015). 3-d joint inversion of the magnetotelluric
 682 phase tensor and vertical magnetic transfer functions. *Geophysical Journal Interna-*
 683 *tional*, 203(2), 1128–1148. doi: 10.1093/gji/ggv347
- 684 Whaler, K., & Hautot, S. (2006). The electrical resistivity structure of the crust beneath
 685 the northern Main Ethiopian Rift. *Geological Society, London, Special Publications*,
 686 259(1), 293–305. doi: 10.1144/GSL.SP.2006.259.01.22
- 687 Wilks, M., Rawlinson, N., Kendall, J. M., Nowacki, A., Biggs, J., Ayele, A., & Wookey,

688 J. (2020). The coupled magmatic and hydrothermal systems of the restless Aluto
689 Caldera, Ethiopia. *Frontiers in Earth Science*, 8(October), 1–14. doi: 10.3389/
690 feart.2020.579699